ChemComm

COMMUNICATION

View Article Online
View Journal | View Issue

Cite this: *Chem. Commun.*, 2025, **61**, 8204

Received 6th February 2025,
Accepted 29th April 2025

DOI: 10.1039/d5cc00660k

rsc.li/chemcomm

Triphenyl phosphonium functionalized amphiphilic peptides as promising antibacterial and anticancer agents†

Tanushree Mondal,[a] Sraddhya Roy,[b] Ananya Das,[b] Sagnik Banerjee,[a] Biplab Mondal,[a] Nabanita Chatterjee[b] and Arindam Banerjee*[a]

Triphenyl phosphonium conjugated amphiphilic peptides are self-assembled into micelles that show potential antimicrobial activity against drug resistant strains. Moreover, these peptides destroy ovarian cancer cells through mitochondrial reactive oxygen species (ROS) generation while maintaining cytocompatibility with HEK 293 (non-cancerous) cells, indicating the emergence of biomaterials with anticancer and antimicrobial activities.

Peptide amphiphiles (PAs) are biomaterials engineered to self-assemble into nanostructures[1] such as nanofibers,[2,3] nanotubes,[4] and micelles,[5] driven by noncovalent interactions. Their structure is influenced by peptide sequence, length, and hydrophobic properties, offering potential in diverse biomedical applications such as mitochondrial targeting and antimicrobial activity.[6,7] Antibiotic resistance, driven by the misuse of antibiotics, is a pressing global challenge.[1–5] Drug-resistant bacteria render traditional treatments ineffective, increasing healthcare costs and mortality.[8,9] The lipophilic TPP cation accumulates in mitochondria, enhancing drug selectivity and efficiency, making it a promising tool for antimicrobial activity against pathogens.[10–12] Novel antimicrobial agents with unique mechanisms, such as PAs and triphenyl phosphine (TPP)-conjugates, offer a promising solution to bypass resistance pathways.[6] TPP-conjugated agents effectively target mitochondrial membranes, demonstrating antiproliferative potency in cancer therapies.[13] Ovarian cancer is the deadliest gynecological malignancy, and often evades the immune system and resists programmed cell death, leading to high recurrence rates and treatment challenges.[14,15] Standard therapies face limitations due to drug resistance and toxicity.[16,17] The TPP conjugated motif offers innovative solutions to enhance drug delivery, target apoptosis, and improve outcomes in cancer therapy.[18,19] We aim to engineer a multifunctional molecule by conjugating a peptide with a TPP group to explore the possibility of dual action against microbial infections and cancer.

In this work we have synthesised two amphiphilic peptides by conjugating TPP motifs, namely TPP–phenylalanine–glycine–dodecylamine (PHFGC12) and TPP–phenylalanine–phenylalanine–dodecylamine (PHFFC12). These two amphiphilic peptides, PHFGC12 (P1) and PHFFC12 (P2) are elegantly self-assembled to form micelles in 1% (v/v) DMSO–water solution at pH 7.0 (Scheme 1). To enhance the peptide self-assembly efficacy we replaced the glycine with hydrophobic L-phenylalanine in P2. Quantitative estimation of the effect of replacing glycine with phenylalanine is an important direction for future research through a computational approach. For effective binding to the negatively charged surface of a microbial lipid membrane, TPP offers an optimal positive charge. Furthermore, a hydrophobic tail was necessary to embed into the interior of the phospholipid membrane. By conjugating TPP with these peptide amphiphiles, it specifically targeted the mitochondria of cancer cells, facilitating selective interactions and disrupting their functions. These

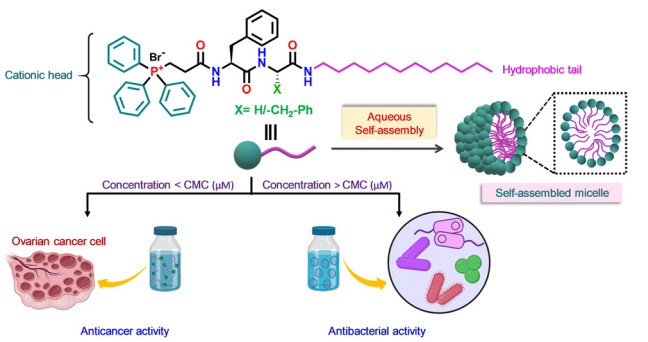

Scheme 1 Diagram depicting the self-assembly of phosphonium-functionalized amphiphilic peptides into micelles, showcasing their antibacterial and anticancer activity.

[a] *School of Biological Sciences, Indian Association for the Cultivation of Science, A2A & 2B Raja S. C. Mullick Road, Jadavpur, Kolkata-700032, India. E-mail: bcab@iacs.res.in*

[b] *Chittaranjan National Cancer Institute, 37 S. P. Mukherjee Road, Kolkata 700026, India*

† Electronic supplementary information (ESI) available. See DOI: https://doi.org/10.1039/d5cc00660k

micelles act as a cell-penetrating nanostructure through self-assembly behaviour in antibacterial studies. When we studied their anticancer properties, P1 and P2 demonstrated potential activity as anticancer agents even below their critical micelle concentration (CMC), as the peptide amphiphiles themselves exhibit inherent anticancer effects. In summary, the conjugation of TPP cations with peptides offers a promising strategy for improving their efficacy in biomedical applications.

The CMC of P1 and P2 was measured by a fluorescence probe assay using a hydrophobic dye Nile red (Fig. 1A and B).[5] The CMC was determined from the intercept of the two linear fitting curves and the calculated values for P1 and P2 were 22 μM and 12 μM, respectively. The lower CMC values for P2 were due to the higher hydrophobicity of phenylalanine than glycine.[5]

Field emission gun transmission electron microscopy (FEG-TEM) was used to characterize the morphology of the peptide amphiphiles in their self-assembled states. FEG-TEM analysis was performed for P1 (25 μM) and P2 (15 μM) in a 1% (v/v) DMSO–water mixture and diluted with Milli-Q water, ensuring the final concentrations above their CMC values. TEM study revealed small spherical micelles for both P1 and P2 with mean diameters ranging from 321 to 326 nm and 220 to 225 nm, respectively (Fig. 1C and D).

Dynamic light scattering (DLS) measurements were conducted to determine the hydrodynamic diameter and the zeta-potential of P1 and P2 in their respective self-assembled state. Stock solutions of P1 (25 μM) and P2 (15 μM) were prepared in a 1% (v/v) DMSO–water mixture. The hydrodynamic diameters measured by DLS (Fig. 1E and F) were in good agreement with the size observed by FEG-TEM (Fig. 1C and D). The zeta-potential values provide insight into the surface charge of the samples. P1 and P2 exhibit positive zeta-potential values of 54 mV and 58 mV, respectively (Fig. 1G). These results indicate that the self-assembled structures of both P1 and P2 possess a phosphonium cation on the surface of the micelles, confirming the generation of cationic charge in their assembled state.[5,6]

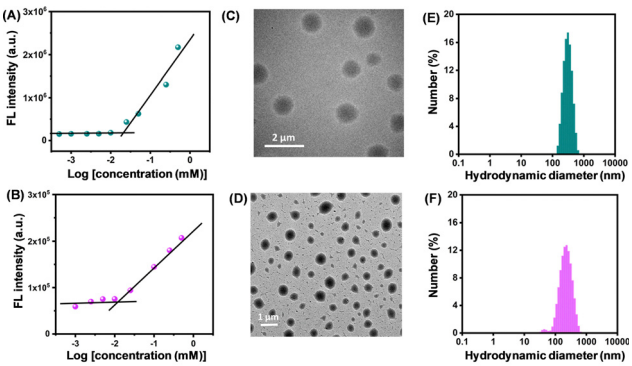

(G)

Name	CMC (μM)	Size (nm)	Zeta Potential (mV)
PHFGC12 (P1)	22	321 ± 5	54 ± 3
PHFFC12 (P2)	12	220 ± 5	58 ± 5

Fig. 1 Critical micelle concentration determination of (A) P1 and (B) P2 in an aqueous medium. FEG-TEM images of (C) P1 and (D) P2 in an aqueous medium. DLS size distribution profile of (E) P1 and (F) P2 in an aqueous medium. (G) Quantitative measurements table of CMC, size distribution and zeta potential values of P1 and P2.

Upon verifying the cell viability (Fig. S13, ESI†) of P1 and P2, their antibacterial activities were tested against four bacterial strains Gram-positive *Bacillus subtilis* (*B. subtilis*) and *Staphylococcus aureus* (*S. aureus*) and Gram-negative *Escherichia coli* (*E. coli*) and *Pseudomonas aeruginosa* (*P. aeruginosa*). Minimum inhibitory concentrations (MICs) were determined through growth absorbance measurements to evaluate antibacterial efficacy. For P1, the MIC values were 63 μM and 62 μM for *P. aeruginosa* and *E. coli* and 60 μM and 52 μM for *B. subtilis* and *S. aureus*, respectively (Table S1, ESI†). In comparison, P2 demonstrated lower MICs, with values of 40 μM and 50 μM for *P. aeruginosa* and *E. coli* and 45 μM and 48 μM for *B. subtilis* and *S. aureus*, respectively (Table S1, ESI†). These results indicate that P2 has stronger antibacterial properties than P1, as evidenced by consistently lower MIC values. A disc diffusion assay was also performed to further evaluate the antibacterial performance of P1 and P2 at the MIC, with photographic images of agar culture plates presented for visualization (Fig. S14A–D, ESI†). In this assay, the zones of inhibition were measured after 24 hours to assess the bactericidal activity. P1 displayed inhibition zones of 18 mm for both *P. aeruginosa* and *E. coli* and 18 mm and 20 mm for *B. subtilis* and *S. aureus* (Table S1, ESI†). Conversely, P2 produced inhibition zones of 22 mm and 18 mm for *P. aeruginosa* and *E. coli* and 20 mm and 18 mm for *B. subtilis* and *S. aureus* (Table S1, ESI†). The above results depict that P2 showed better antibacterial efficacy than P1. These results confirm that P2 shows enhanced antibacterial efficacy, particularly against Gram-negative bacteria, likely due to its stronger inhibitory action on Gram-negative bacteria.

Field emission scanning electron microscopy (FE-SEM) is a widely used technique for directly observing bacterial surface morphology. The FE-SEM images of *S. aureus*, *B. subtilis*, *P. aeruginosa*, and *E. coli* showed partial membrane damage and rupture compared to the untreated control, which displayed a bright and smooth surface (Fig. S14E–H, ESI†). Bacterial cells that have undergone membrane damage lose their typical shape (Fig. S14I–L, ESI†). More pronounced membrane rupture and leakage of cell contents were observed in the treated samples. These SEM studies can indicate membrane disruption in the bacterial cell surface, through holes, rough surfaces, and irregular shapes.

The live/dead bacterial assay using propidium iodide (PI) and SYTO 9 is a widely used method to distinguish between live and dead bacterial cells. SYTO 9 is a green fluorescent nucleic acid stain dye that can penetrate both live and dead bacterial cells, while PI is a red fluorescent nucleic acid stain dye that only enters cells with compromised membranes, marking them as dead.[2,11] This selective entry makes PI useful for identifying non-viable cells in a mixed population. When stained with the SYTO 9 and PI combination, viable cells with intact membranes fluoresce green, while cells with compromised membranes fluoresce red, indicating membrane damage or cell death. This technique is particularly valuable for studying the effects of membrane-active agents. In this study, *S. aureus* and *P. aeruginosa* cells were treated with compound P2 at its minimum inhibitory concentration. Following the dye treatment, the cells were stained with SYTO 9 and PI and these cells were imaged to assess the effect of P2 on bacterial

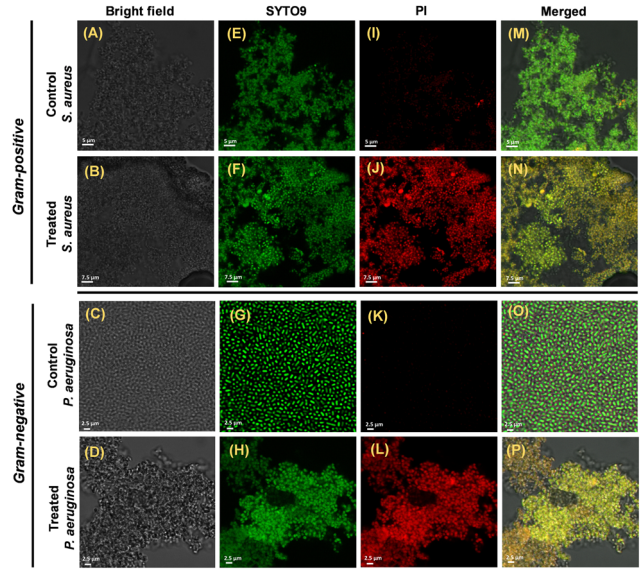

Fig. 2 Confocal microscopic images of live/dead assay of *S. aureus* and *P. aeruginosa* with P2 (Treated) and without P2 (Control). Bright field (A–D); SYTO9 stained green zones (E–H); PI stained red zones (I–L) and merged (M–P) respectively.

cell membranes (Fig. 2E–P). Untreated control cells, with intact membranes, appeared green in merged images (Fig. 2M and O), which is indicated by the lack of any overlap with the red dye, signifying viable cells. In contrast, cells treated with P2 displayed red fluorescence (Fig. 2J and L), indicating disrupted, lysed, or compressed membranes and the merged images of yellow emission (Fig. 2N and P) from the overlap of both green and red dye provide clear evidence of post-treatment bacterial cell death.

To investigate the antibacterial mechanisms, we conducted membrane disruption assays targeting both the outer (Fig. S15, ESI†) and inner (Fig. S16 and S17, ESI†) bacterial membranes.[2,12] At the MIC, the outer membrane permeability of peptides P1 and P2 exceeded 60%, reaching nearly 80% at double the minimum inhibitory concentration (2MIC) (Fig. S15, ESI†). For *P. aeruginosa*, inner membrane permeability surpassed 60% at the 2MIC, while for *S. aureus*, permeability exceeded 70% at the MIC and nearly 80% at the 2MIC (Fig. S16 and S17, ESI†). These findings confirm that P1 and P2 primarily exert antibacterial effects through membrane disruption (Fig. S18, ESI†). Amphiphilic peptides like P1 and P2 interact electrostatically with negatively charged bacterial membranes, followed by hydrophobic tail insertion into the lipid bilayer, leading to depolarization, destabilization, and cell death.[11,12] In 1% (v/v) DMSO–water, nanostructures enhance peptide aggregation, increase local charge density and promote bacterial membrane binding. This mechanism supports outer membrane disruption in Gram-negative bacteria and inner membrane damage in both Gram-negative and Gram-positive bacteria. Field-emission scanning electron microscopy and live/dead staining assays confirmed membrane damage. While P1 and P2 share structural similarities, P2's additional phenylalanine group increases hydrophobicity, enhancing its antimicrobial potency. Our findings highlight that both self-assembly and membrane disruption are essential for the strong antibacterial activity of these peptide amphiphiles.

To evaluate the cytotoxicity of compounds P1 and P2, an MTT assay was conducted on ovarian adenocarcinoma cells (SKOV3) and normal human epithelial cells (HEK 293). The results revealed a pronounced cytotoxic effect on SKOV3 cells, with IC_{50} values of 1.350 μM for P1 and 1.162 μM for P2 found in a dose-dependent manner for 24 hours (Fig. S19A and B, ESI†). P2 demonstrated greater potency, significantly reducing SKOV3 cell viability ($P < 0.001$) compared to P1 ($P < 0.05$). Consequently, further experiments focused on P2. Treated SKOV3 cells exhibited nuclear fragmentation and distortion compared to controls, emphasizing P2's cytotoxic efficacy (Fig. S19C, ESI†). These findings highlight the selective impact of P2 on cancer cells while sparing normal cells, making it a promising candidate for further investigation. In contrast, minimal cytotoxicity was observed in HEK 293 cells, which remained viable even at 500 μM (Fig. S13A and B, ESI†).

To understand the underlying facts inducing greater apoptotic cells, we have explored mitochondrial protein cytochrome *c* (Cyt *c*) and reactive oxygen species (ROS) generation. Upon deducing that the ROS level has increased under the treatment of P2 at a significance of $P < 0.001$ (Fig. S20A, ESI†), we were inclined to study the Cyt *c* levels. The results revealed increased Cyt *c* levels in the treated cells compared to the control cells at a significance of $P < 0.01$ (Fig. S20B, ESI†), indicating that the increased ROS is a result of elevated Cyt *c* in the treated cells. Upon deducing this, when we analyzed annexinV+ cells under the treatment, it was observed that the apoptotic cells were higher under the treated condition with a significance level of $P < 0.001$ (Fig. S20C, ESI†). Increased ROS upon the higher secretion of Cyt *c* increases the apoptotic rate of the cancer cells. On evaluating the expression of the pro-apoptotic marker, Bax, (Fig. 3A and Fig. S21a, ESI†) and anti-apoptotic marker, Bcl2 (Fig. 3B and Fig. S21b, ESI†) by flow cytometry, it was depicted that the Bax level was increased in the treated cells in comparison to the control cells ($P < 0.001$) and the Bcl2 level decreased considerably ($P < 0.01$). To evaluate the involvement of caspases in the apoptotic processes, *i.e.* the intrinsic and extrinsic pathway, it was observed that caspase 9, which regulates the intrinsic pathway, was significantly higher in comparison to caspase 8, which drives the extrinsic pathway in the treated cells ($P < 0.001$). Furthermore, it

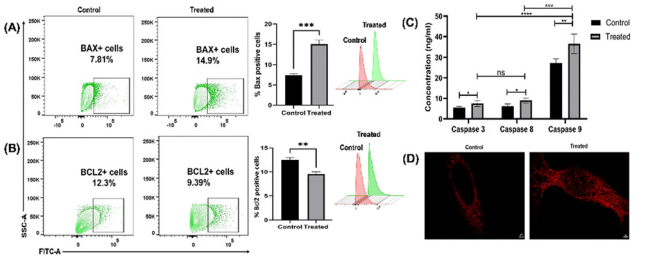

Fig. 3 Flow cytometric and enzyme analysis of apoptotic proteins with the treatment of P2. (A) Flow cytometric analysis of pro-apoptotic, Bax+ cells. (B) Flow cytometric analysis of anti-apoptotic, Bcl2+ cells. (C) Analysis of caspases secreted by SKOV3 cells by ELISA. (D) Confocal imaging of APAF-1 expression (*$P < 0.1$, **$P < 0.01$, ***$P < 0.001$, ****$P < 0.0001$).

was illustrated that P2 could have induced caspase 9 followed by the caspase 3 dependent pathway ($P < 0.001$), whereas the involvement of caspase 8 is not significant (Fig. 3C). This may lead to the intrinsic mitochondrial dependent pathway. Additionally, upon analysing the expression of apoptotic protease activating factor 1 (APAF-1), a prime molecule of intrinsic apoptotic signalling, it was observed that upon treatment with P2 the nuclear localization of APAF-1 increased considerably as compared with the control (Fig. 3D). Using JC-1 staining, we found that P2 selectively reduced mitochondrial membrane potential in SKOV3 cancer cells without affecting HEK293 normal cells, while P1 showed no significant effect (Fig. S22, ESI†).

Apoptosis, a programmed cell death mechanism, is mediated by caspases and is crucial for maintaining cellular homeostasis. Apoptosis involves two pathways: the mitochondria-dependent intrinsic pathway and the receptor-dependent extrinsic pathway. The intrinsic pathway is regulated by the Bcl-2 protein family, comprising pro-apoptotic members (*e.g.*, Bax, Bak, Bid) and anti-apoptotic members (*e.g.*, Bcl-2, Bcl-XL).[14,15] This study focused on the intrinsic pathway, as increased ROS levels were observed in treated cells. Elevated ROS, generated through mitochondrial and endoplasmic reticulum crosstalk, can signal growth at low levels but induce apoptosis at higher levels by damaging cellular components.[19] Elevated ROS promotes Cyt *c* secretion into the cytosol, where it forms apoptosomes with APAF-1, activating caspase-9 and downstream caspases-3.[18,20] Our results demonstrated significantly increased Cyt *c* and caspase activity in treated cells. Additionally, Bax levels were elevated, while anti-apoptotic Bcl-2 levels were reduced in treated cells compared to controls. AnnexinV staining further confirmed increased apoptotic cells in treated samples. These findings suggest that P2 more effectively induces apoptosis in ovarian cancer cells by activating the intrinsic pathway. Elevated ROS levels, Cyt *c* secretion, and modulation of Bcl-2 family proteins collectively highlight the intrinsic cascade's role in apoptosis. In this context, we can illustrate that P2 is a potent drug to induce apoptosis in the ovarian cancer cells by activating the intrinsic pathway of apoptosis.

In conclusion, TPP-functionalized amphiphilic peptides P1 and P2 were synthesized and self-assembled into micelles in 1% (v/v) DMSO–water. Micellar structures were characterized using CMC determination, DLS, and TEM. The peptides demonstrated excellent biocompatibility, with phosphonium functionalization enhancing micelle formation and facilitating cell targeting. Additionally, P1 and P2 showed significant antibacterial activity against Gram-positive (*B. subtilis*, *S. aureus*) and Gram-negative (*E. coli*, *P. aeruginosa*) bacteria. Their bactericidal efficacy, confirmed through SEM imaging and membrane disruption assays, highlights their potential in combating antibiotic-resistant bacteria. This study establishes P1 and P2 micelles as promising candidates for addressing global antibacterial resistance challenges. Mechanistic studies revealed that P2 selectively eradicated SKOV3 cancer cells *via* caspase-mediated apoptosis, driven by elevated intracellular ROS levels, nuclear morphological changes, and activation of the intrinsic apoptosis pathway. This candidate could be established as a newer entity with therapeutic prospects in ovarian cancer.

T. M., S. B., A. D., wish to acknowledge the Council of Scientific & Industrial Research (CSIR-India); B. M. acknowledges IACS for the support. S. R. acknowledges the University Grants Commission, Govt. of India for financial support.

Data availability

The supporting data including instrumentation, materials and methods, synthetic scheme, synthesis procedure, HR-MS, ^{1}H NMR, ^{13}C NMR and ^{31}P NMR spectroscopy, methods of antibacterial and anticancer studies, and cell viability assessment, have been included as a part of the ESI.†

Conflicts of interest

The authors declare no conflict of interest.

Notes and references

1 R. Singh, S. Sharma, A. Kautu and K. B. Joshi, *Chem. Commun.*, 2024, **60**, 7687–7696.
2 L. Colomina-alfaro, P. Sist, P. D. Andrea, R. Urbani, S. Marchesan and A. Bandiera, *J. Mater. Chem. B*, 2024, **12**, 8966–8976.
3 T. Mondal, A. Chatterjee, B. Hansda, B. Mondal, P. Sen and A. Banerjee, *Soft Matter*, 2024, **20**, 1236–1244.
4 L. Schnaider, S. Brahmachari, N. W. Schmidt, B. Mensa, S. Shaham-Niv, D. Bychenko, L. Adler-Abramovich, L. J. W. Shimon, S. Kolusheva, W. F. Degrado and E. Gazit, *Nat. Commun.*, 2017, **8**, 1365.
5 L. Xiao, J. Zho, J. D. London, J. D. Pochan and X. Jia, *Soft Matter*, 2012, **8**, 10233–10237.
6 B. Hisey, P. J. Ragogna and E. R. Gillies, *Biomacromolecules*, 2017, **18**, 914–923.
7 C. C. Piras, C. S. Mahon and D. K. Smith, *Chem. – Eur. J.*, 2020, **26**, 8452–8457.
8 Q. Zhang, W. Tan, Z. Liu, Y. Zhang, W. Wei, S. Fraden and B. Xu, *J. Am. Chem. Soc.*, 2024, **146**, 12901–12906.
9 D. Ghosh, S. M. Coulter, G. Laverty, C. Holland, J. J. Doutch, M. Vassalli and D. J. Adams, *Biomacromolecules*, 2024, **25**, 3169–3177.
10 M. C. Giano, Z. Ibrahim, S. H. Medina, K. A. Sarhane, J. M. Christensen, Y. Yamada, G. Brandacher and J. P. Schneider, *Nat. Commun.*, 2014, **5**, 4095.
11 N. R. De Almeida, Y. Han, J. Perez, S. Kirkpatrick, Y. Wang and M. C. Sheridan, *ACS Appl. Mater. Interfaces*, 2019, **11**, 2790–2801.
12 K. J. Sommers, M. E. Michaud, C. E. Hogue, A. M. Scharnow, L. E. Amoo, A. A. Petersen, R. G. Carden, K. P. C. Minbiole and W. M. Wuest, *ACS Infect. Dis.*, 2022, **8**, 387–397.
13 S. S. Liew, X. Qin, J. Zhou, L. Li, W. Huang and S. Q. Yao, *Angew. Chem., Int. Ed.*, 2021, **60**, 2232–2256.
14 B. R. Rueda, *Cancers*, 2019, **11**, 1–27.
15 L. A. Torre, B. Trabert, C. E. Desantis, K. D. Miller, G. Samimi, C. D. Runowicz, M. M. Gaudet and A. Jemal, *CA. Cancer J. Clin.*, 2018, **68**, 284–296.
16 H. Xie, L. Song, S. Katz, J. Zhu, Y. Liu, J. Tang and L. Cai, *Redox Biol.*, 2022, **53**, 102340.
17 S. Das, N. Chatterjee and D. Bose, *Tumor Biol.*, 2015, **36**, 3109–3118.
18 L. Qi, Q. Luo, Y. Zhang, F. Jia, Y. Zhao and F. Wang, *Chem. Res. Toxicol.*, 2019, **32**, 1469–1486.
19 R. Article, *Cancer Sci.*, 2021, **112**, 3945–3952.
20 Y. P. Ow, D. R. Green, Z. Hao and T. W. Mak, *Nat. Rev. Mol. Cell Biol.*, 2008, **9**, 532–542.